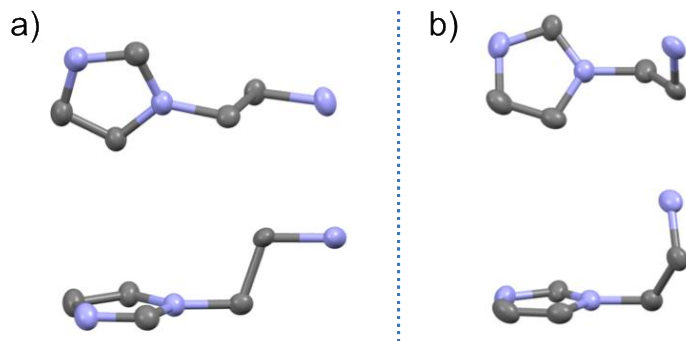


## Supporting Information

### Formation of Corrugated $n = 1$ 2D Tin Iodide Perovskites and Their Use as Lead-Free Solar Absorbers

Benny Febriansyah,<sup>[a],[b],[c]</sup> Yulia Lekina,<sup>[d]</sup> Jagjit Kaur,<sup>[e]</sup> Thomas J. N. Hooper,<sup>[f]</sup> Padinhare Cholakkal Harikesh,<sup>[b],[c]</sup> Teddy Salim,<sup>[g]</sup> Ming Hui Lim,<sup>[a]</sup> Teck Ming Koh,<sup>[b]</sup> Sudip Chakraborty,<sup>[e]\*</sup> Ze Xiang Shen,<sup>[b],[d]\*</sup> Nripan Mathews,<sup>[b],[g]\*</sup> Jason England<sup>[a]\*</sup>

- [a] Division of Chemistry and Biological Chemistry, School of Physical and Mathematical Sciences, Nanyang Technological University, 21 Nanyang Link, Singapore 637371, Singapore.
- [b] Energy Research Institute at Nanyang Technological University (ERI@N), Research Techno Plaza, X-Frontier Block Level 5, 50 Nanyang Drive, Singapore 637553, Singapore.
- [c] Interdisciplinary Graduate School (IGS), 50 Nanyang Avenue, Singapore 639798 Singapore.
- [d] Division of Physics and Applied Physics, School of Physical and Mathematical Sciences, Nanyang Technological University, 21 Nanyang Link, Singapore 637371, Singapore.
- [e] Materials Theory for Energy Scavenging (MATES) Lab, Discipline of Physics, Indian Institute of Technology Indore, Simrol, Indore 453552, India.
- [f] Centre of High Field NMR Spectroscopy and Imaging, Nanyang Technological University, 21 Nanyang Link, Singapore 637371, Singapore.
- [g] School of Materials Science and Engineering, Nanyang Technological University, 50 Nanyang Avenue, Singapore 639798, Singapore.



**Figure S1.** Top and side views of the two distinct  $\text{ImEA}^{2+}$  dications (a and b) in the X-ray crystal structure of the corrugated 2D perovskite  $\text{ImEA}[\text{SnI}_4]$ . Grey and blue spheroids represent C and N atoms, respectively. H atoms are omitted for clarity. Thermal ellipsoids are shown at 50 % probability.

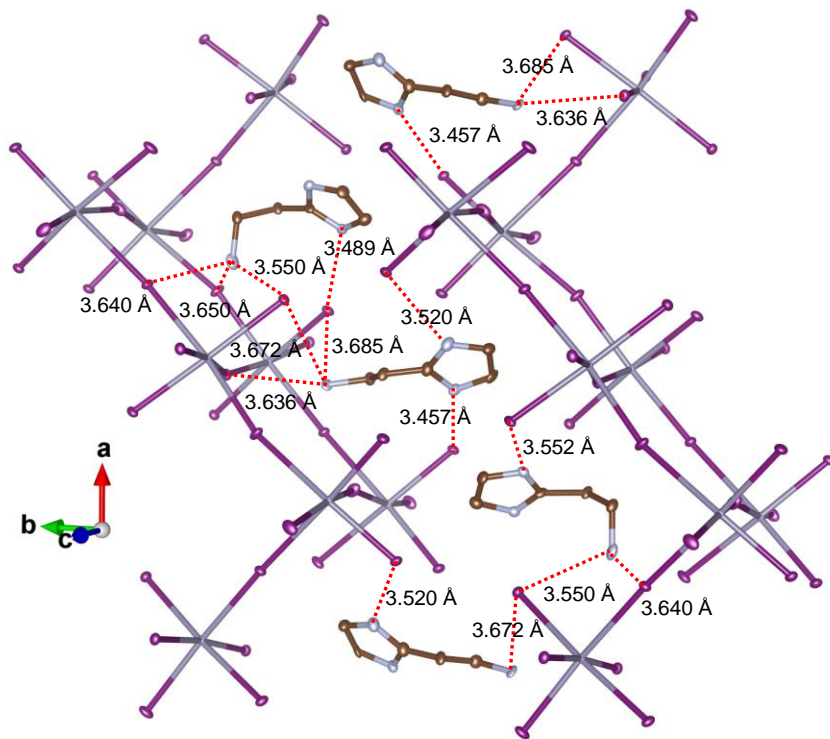


**Figure S2.** X-ray crystal structure of  $\text{2-ImEA}[\text{SnI}_4]$  highlighting the closest contacts between the N-atoms of the primary ammonium and imidazolium  $\text{NH}^+$  functionality of  $\text{2-ImEA}^{2+}$  and the bridging/terminal  $\text{I}^-$  ions of the iodostannate lattice (dashed red lines). Lavender, purple, light brown and blue spheroids correspond to Sn, I, C and N atoms, respectively. H atoms are omitted for clarity. Thermal ellipsoids are shown at 50 % probability.

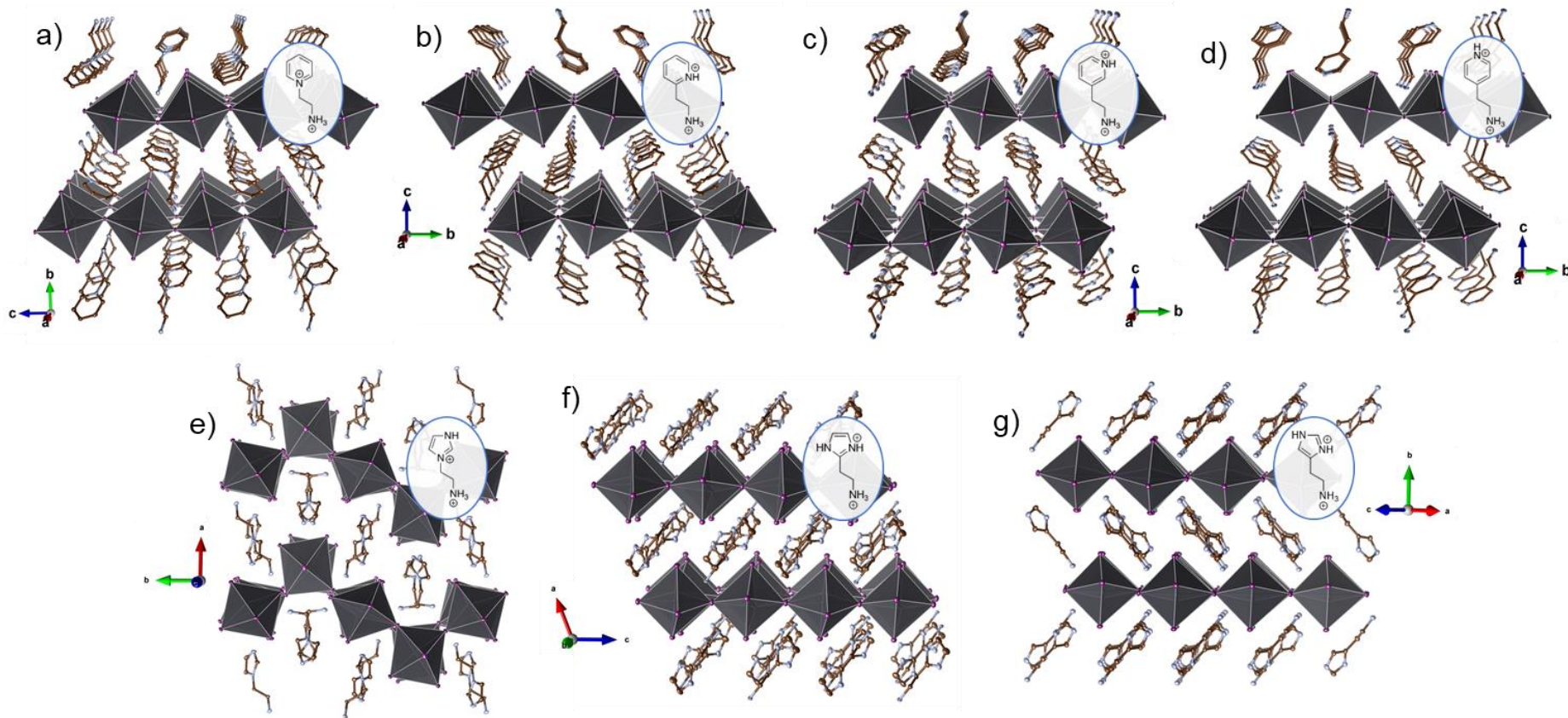


**Figure S3.** X-ray crystal structures of the (100)-oriented 2D lead iodide perovskites a) PyrEA[PbI<sub>4</sub>], b) 2-PyrEA[PbI<sub>4</sub>], c) 3-PyrEA[PbI<sub>4</sub>], d) 4-PyrEA[PbI<sub>4</sub>], f) 2-ImEA[PbI<sub>4</sub>], and g) HA[PbI<sub>4</sub>], and the (110)-oriented congener e) ImEA[PbI<sub>4</sub>]. Dark grey, purple, light brown and light blue spheroids correspond to Pb, I, C and N atoms, respectively. H atoms are omitted for clarity. Thermal ellipsoids are shown at 50 % probability. The insets show the molecular structures of the templating dications. The structures of PyrEA[PbI<sub>4</sub>], ImEA[PbI<sub>4</sub>], and HA[PbI<sub>4</sub>] are taken from ref. 1, while those of 2-PyrEA[PbI<sub>4</sub>], 3-PyrEA[PbI<sub>4</sub>], and 4-PyrEA[PbI<sub>4</sub>] are from ref. 2.

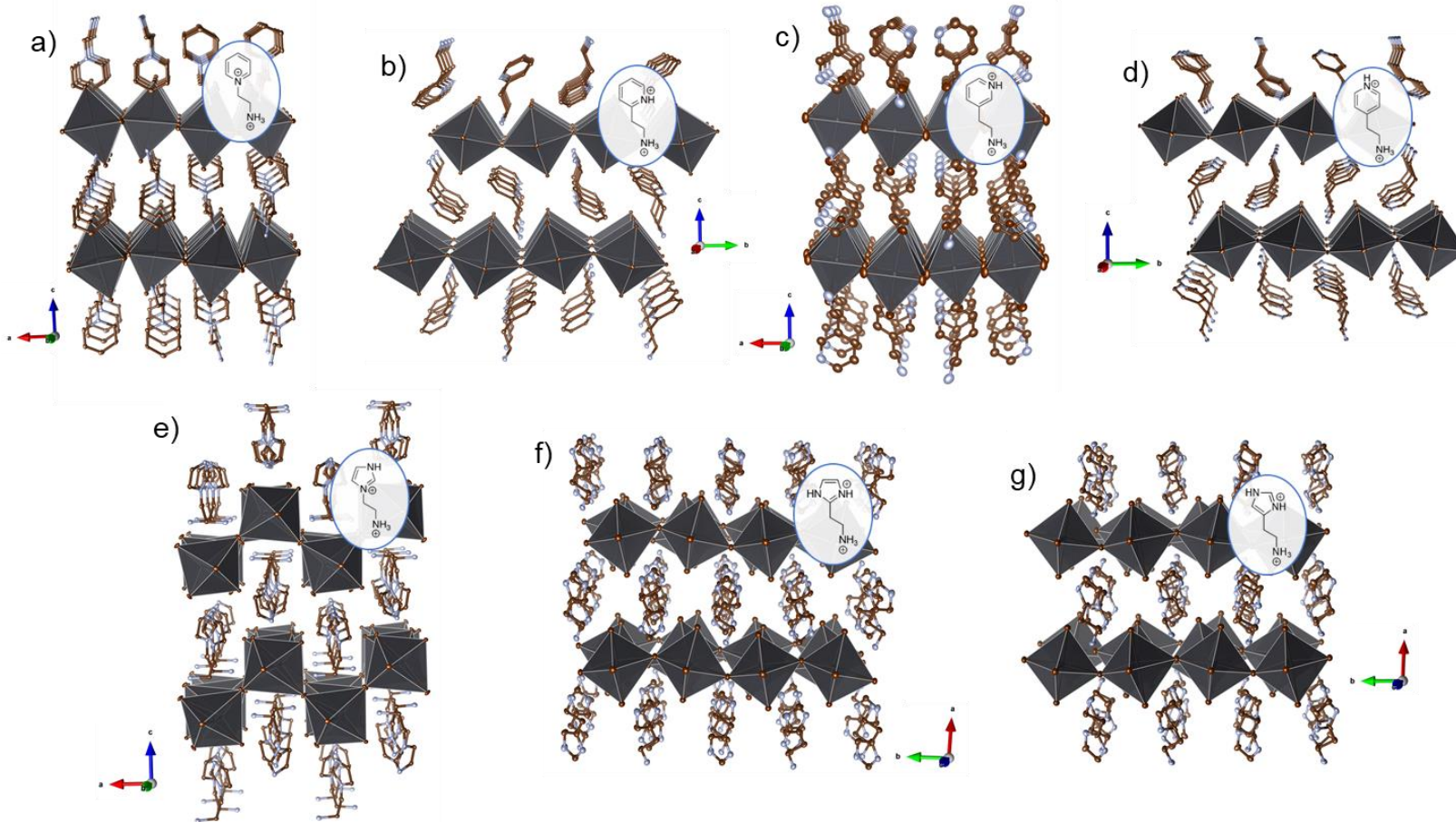


**Figure S4.** X-ray crystal structures of the (100)-oriented 2D lead bromide perovskites a) PyrEA[PbBr<sub>4</sub>], b) 2-PyrEA[PbBr<sub>4</sub>], c) 3-PyrEA[PbBr<sub>4</sub>], d) 4-PyrEA[PbBr<sub>4</sub>], f) 2-ImEA[PbBr<sub>4</sub>], and g) HA[PbBr<sub>4</sub>], and the (110)-oriented congener e) ImEA[PbBr<sub>4</sub>]. Dark grey, dark brown, light brown and light blue spheroids correspond to Pb, Br, C and N atoms, respectively. H atoms are omitted for clarity. Thermal ellipsoids are shown at 50 % probability. The insets show the molecular structures of the templating dications. The structure of PyrEA[PbBr<sub>4</sub>] is taken from ref. 3, while those of 3-PyrEA[PbBr<sub>4</sub>], 4-PyrEA[PbBr<sub>4</sub>], ImEA[PbBr<sub>4</sub>], 2-ImEA[PbBr<sub>4</sub>], and HA[PbBr<sub>4</sub>] are from ref. 4.

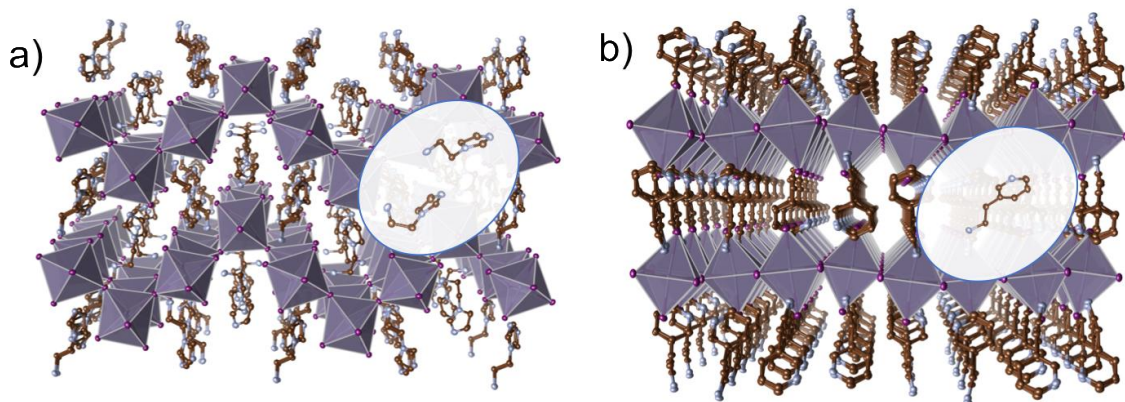


**Figure S5.** X-ray crystal structures of a) (110)-oriented ImEA[SnI<sub>4</sub>] and b) (100)-oriented 3-PyrEA[SnI<sub>4</sub>]. Insets depict the different conformations of their respective templating organic dications. Lavender, purple, light brown and blue spheroids correspond to Sn, I, C and N atoms, respectively. H atoms are omitted for clarity. Thermal ellipsoids are shown at 50 % probability.

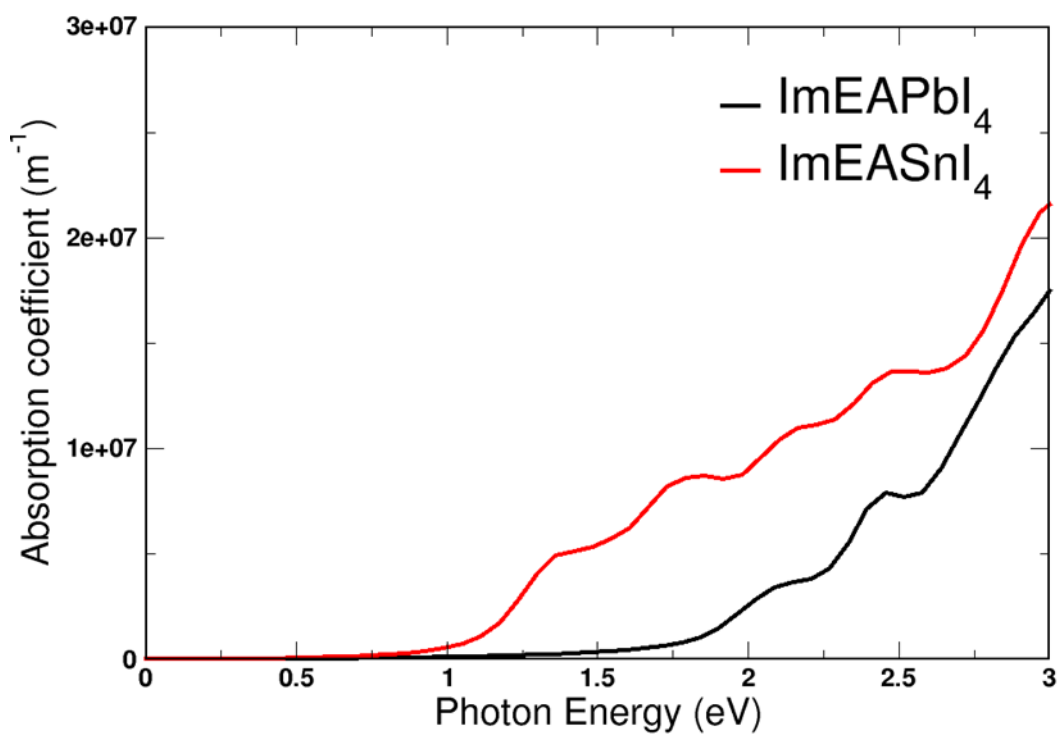


**Figure S6.** DFT calculated UV-Vis absorption spectra of ImEA[PbI<sub>4</sub>] and ImEA[SnI<sub>4</sub>].

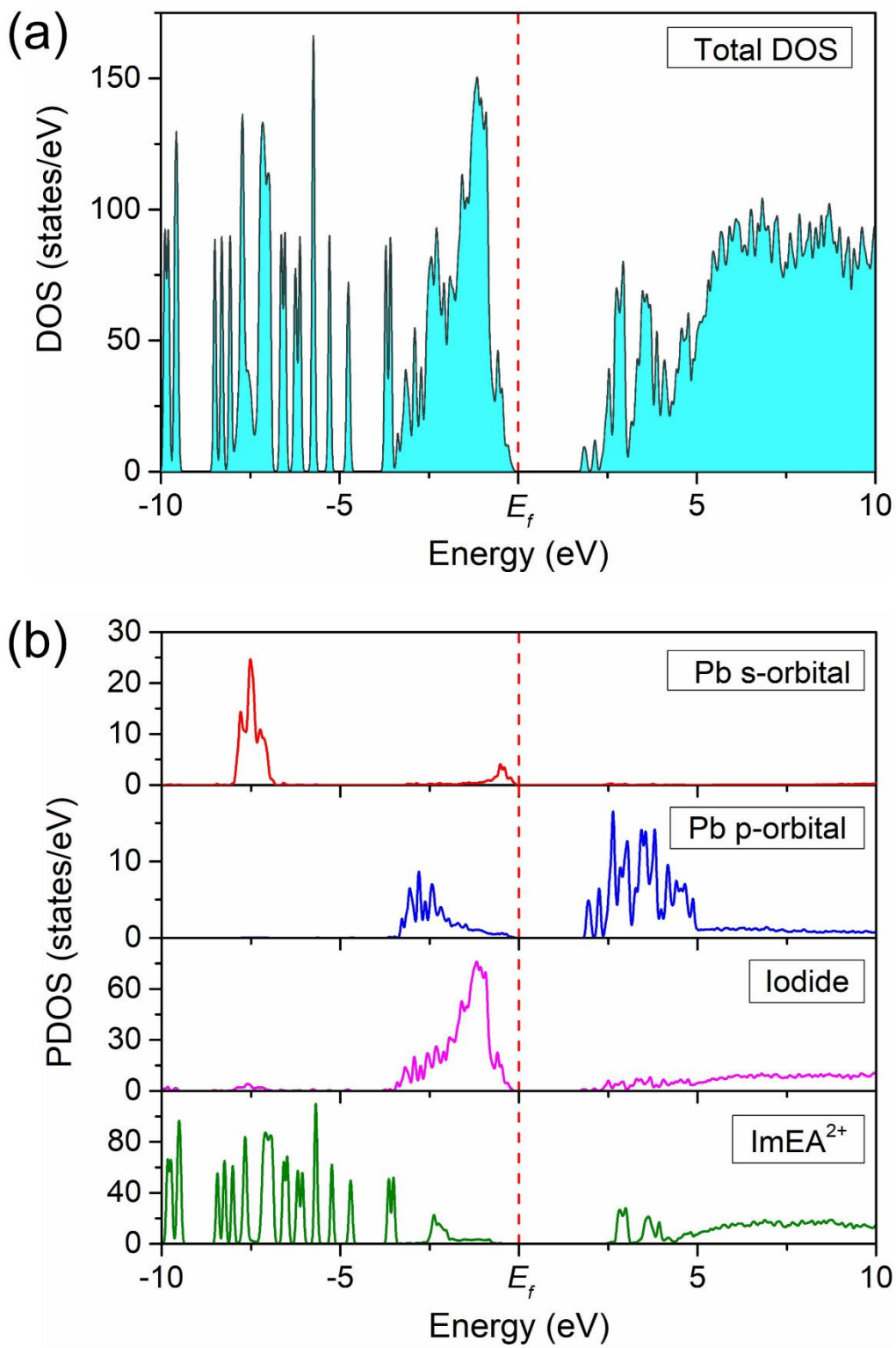


**Figure S7.** DFT calculated a) total density of states (DOS) and b) projected density of states (PDOS) for  $\text{ImEA}[\text{PbI}_4]$ , where  $E_f$  corresponds to the Fermi level.

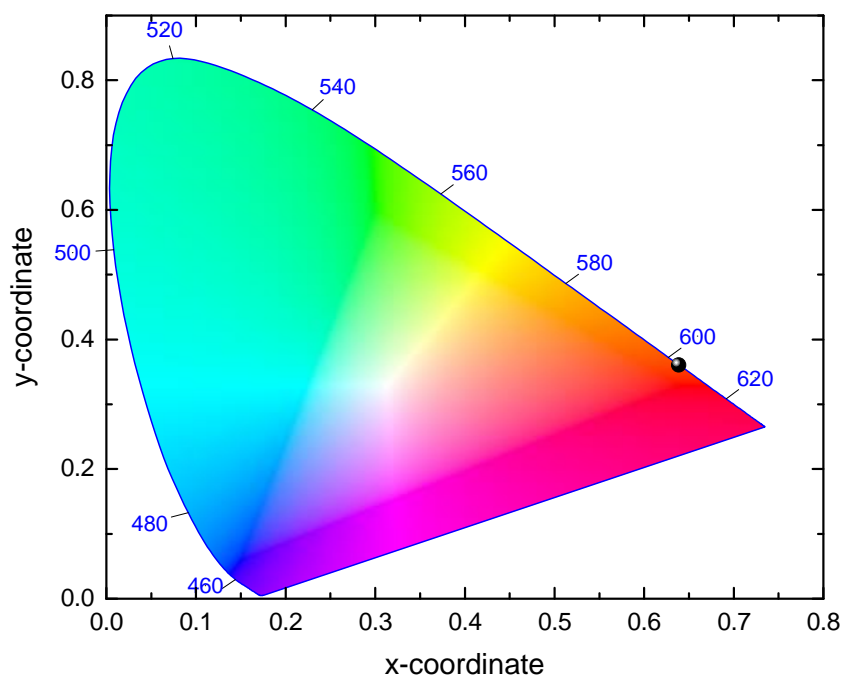


**Figure S8.** Chromaticity coordinates (0.64, 0.36) for the room temperature photoluminescence (PL) emission of ImEA[SnI<sub>4</sub>], depicted using a black sphere.

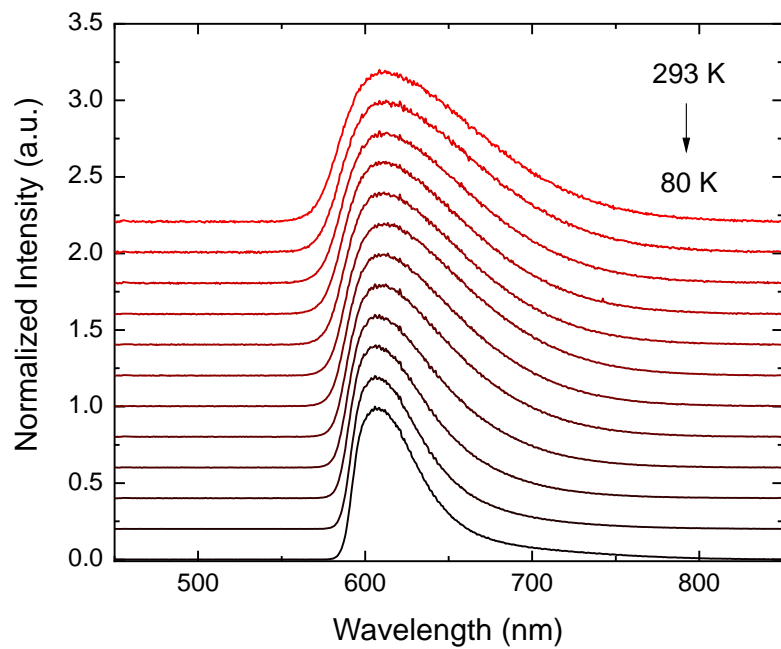


**Figure S9.** Temperature-dependent PL spectra (normalized intensity) of single crystal ImEA[SnI<sub>4</sub>], recorded using a 573 nm continuous-wave laser.

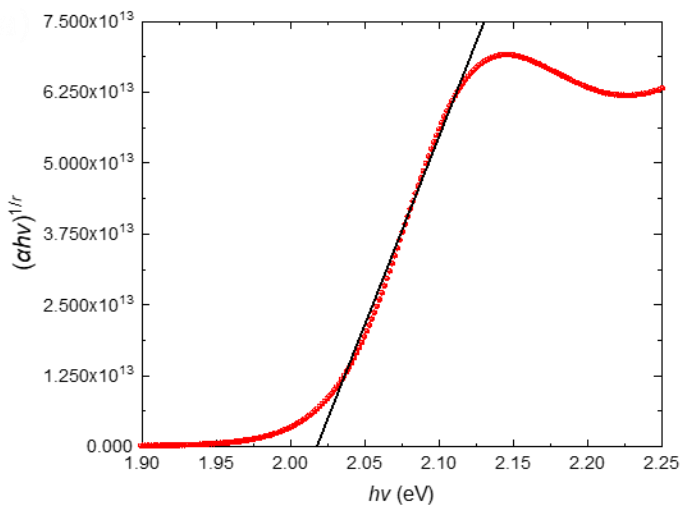


**Figure S10.** Tauc plot of ImEA[SnI<sub>4</sub>], converted from the absorption spectrum of a *ca.* 400 nm thick thin film sample, assuming a direct, dipole-allowed transition ( $r = \frac{1}{2}$ ). The black line is an extrapolation of the linear part of the curve, which corresponds to the band gap of the material.

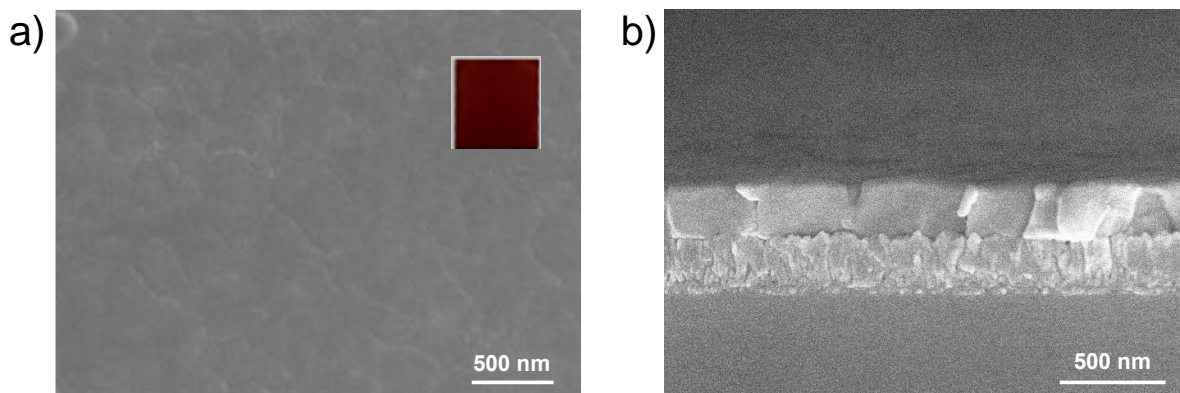


**Figure S11.** Field emission scanning electron micrograph (FESEM) of a) the surface morphology of a spin coated sample of ImEA[SnI<sub>4</sub>], showing complete coverage by a pinhole-free thin film, plus an inset displaying the visual appearance of a spin-coated film; and b) cross-sectional view of a typical ImEA[SnI<sub>4</sub>] thin film, which has a thickness of *ca.* 300 nm.

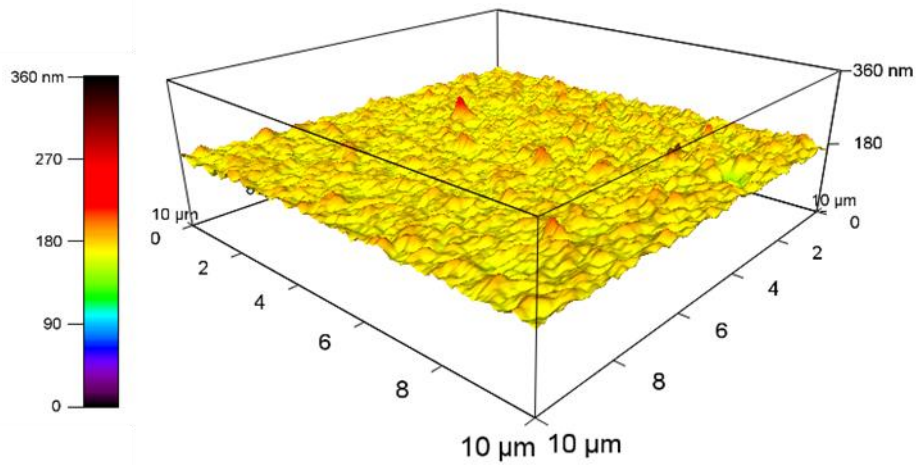


**Figure S12.** Topological image of the surface of an ImEA[SnI<sub>4</sub>] film recorded using atomic force microscopy (AFM). Surface area =  $10 \times 10 \mu\text{m}^2$ . Average film roughness = 14 nm, which is indicative of a very smooth surface.

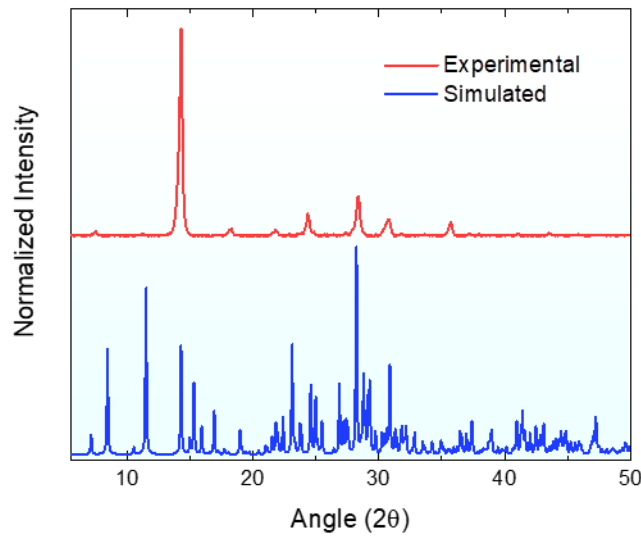


**Figure S13.** Glancing-angle X-ray diffraction (GAXRD) pattern of an ImEA[SnI<sub>4</sub>] film, showing a strong crystallization tendency along (002) orientation. For comparison, the powder XRD pattern simulated using the single crystal X-ray structure of ImEA[SnI<sub>4</sub>] is also included.

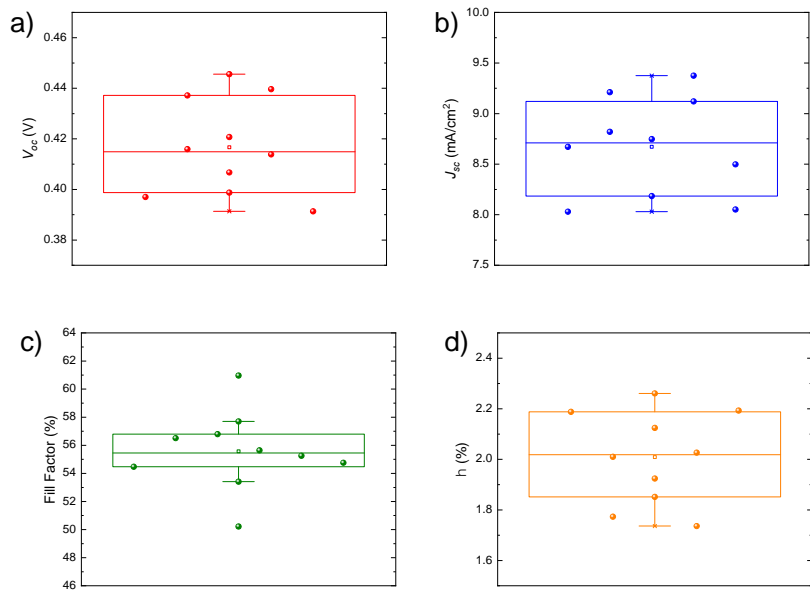


**Figure S14.** Statistical representations of the parameters a) open-circuit voltage ( $V_{oc}$ ), b) short-circuit current density ( $J_{sc}$ ), c) fill-factor ( $FF$ ), and d) power conversion efficiency ( $\eta$ ) measured for 10 photovoltaic devices incorporating the solar absorber ImEA[SnI<sub>4</sub>].

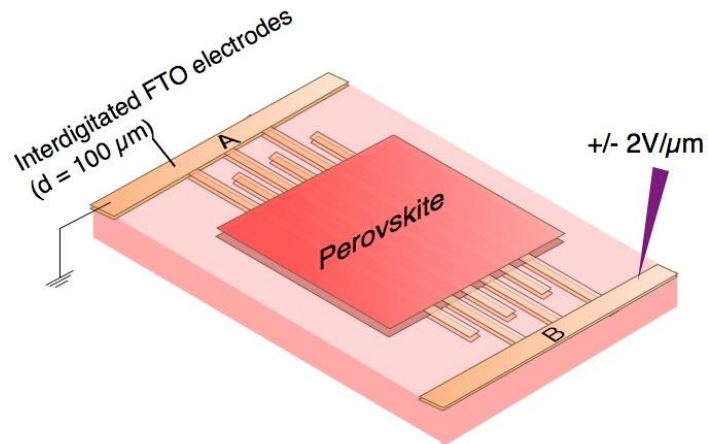


**Figure S15.** Schematic of the lateral device configuration featuring interdigitated electrodes, which was used in poling measurements for ImEA[SnI<sub>4</sub>].

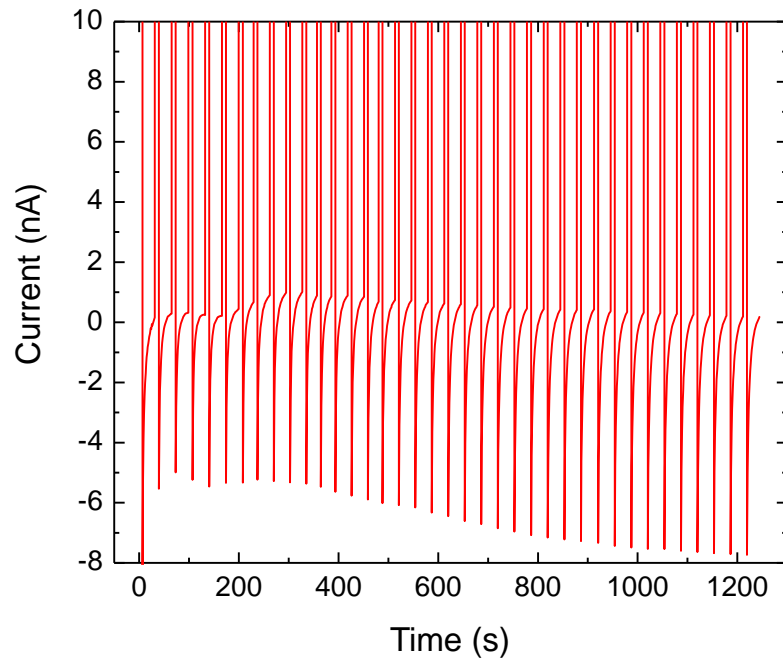


**Figure S16.** Response of the material during application of a pulsed field of  $2 \text{ V } \mu\text{m}^{-1}$ .

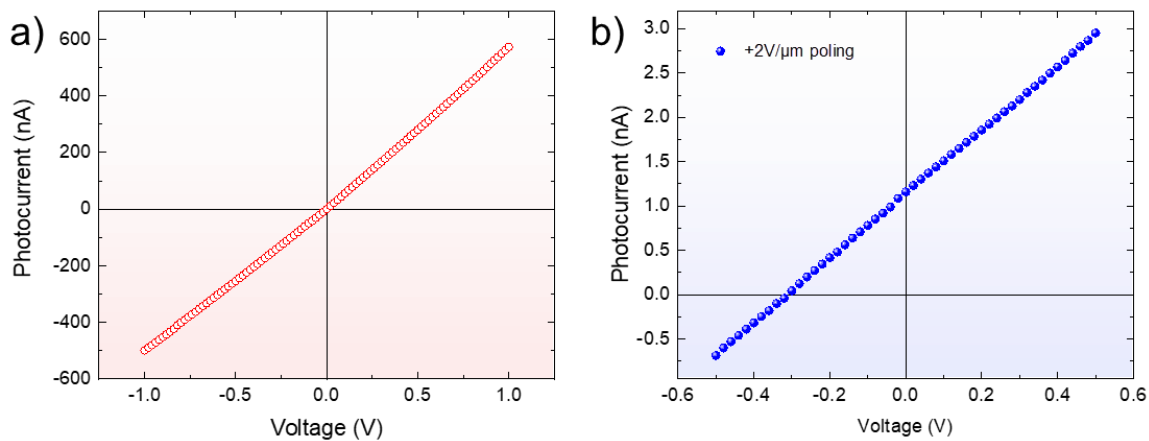


**Figure S17.**  $I$ - $V$  curve of the lateral device before and after  $2 \text{ V } \mu\text{m}^{-1}$  poling, under illumination of 445 nm LED with a power of  $1.4 \text{ mW mm}^{-2}$ .

**Table S1.** Crystallographic and structure refinement data for ImEA[SnI<sub>4</sub>] and 2-ImEA[SnI<sub>4</sub>].<sup>a</sup>

	Compound		
	ImEA[SnI <sub>4</sub> ]	2-ImEA[SnI <sub>4</sub> ]	HA[SnI <sub>4</sub> ]
Empirical formula	C <sub>5</sub> H <sub>11</sub> I <sub>4</sub> N <sub>3</sub> Sn	C <sub>10</sub> H <sub>21</sub> I <sub>8</sub> N <sub>6</sub> Sn <sub>2</sub>	C <sub>5</sub> H <sub>11</sub> I <sub>4</sub> N <sub>3</sub> Sn
Formula weight	739.46 g mol <sup>-1</sup>	1477.91 g mol <sup>-1</sup>	739.46 g mol <sup>-1</sup>
Temperature	100(2) K	100(2) K	100(2) K
Wavelength	0.71073 Å	0.71073 Å	0.71073 Å
Crystal size	0.020 x 0.040 x 0.060 mm	0.300 x 0.320 x 0.400 mm	0.010 x 0.080 x 0.100 mm
Crystal habit	black plate	orange plate	brown plate
Crystal system	monoclinic	orthorhombic	monoclinic
Space group	P 1 21/c 1	P c a 21	P 1 21/c 1
Unit cell dimensions	a = 12.4594(4) Å α = 90° b = 19.6278(7) Å β = 96.2023(16)° c = 12.4690(6) Å γ = 90°	a = 18.8341(9) Å α = 90° b = 13.0740(11) Å β = 90° c = 12.4166(9) Å γ = 90°	a = 12.3596(6) Å α = 90° b = 26.0329(14) Å β = 91.828(2)° c = 28.9180(16) Å γ = 90°
Volume	3031.5(2) Å <sup>3</sup>	3057.4(4) Å <sup>3</sup>	9299.8(8) Å <sup>3</sup>
Z	8	4	24
Density	3.240 g cm <sup>-3</sup>	4.096 g cm <sup>-3</sup>	3.169 g/cm <sup>3</sup>
Absorption coefficient	9.805 mm <sup>-1</sup>	9.773 mm <sup>-1</sup>	9.588 mm <sup>-1</sup>
F(000)	2592	3440	7776
Theta range for data collection	2.43 to 29.16°	1.56 to 30.55°	2.27 to 26.38°
Reflections collected	26259	19147	19087
Coverage of independent reflections	99.5 %	98.4 %	99.3%
Absorption correction	Multi-Scan	Multi-Scan	Multi-Scan
Max. and min. transmission	0.8280 and 0.5910	0.1580 and 0.1110	0.9100 and 0.4470
Function minimized	Σ w(F <sub>o</sub> <sup>2</sup> - F <sub>c</sub> <sup>2</sup> ) <sup>2</sup>	Σ w(F <sub>o</sub> <sup>2</sup> - F <sub>c</sub> <sup>2</sup> ) <sup>2</sup>	Σ w(F <sub>o</sub> <sup>2</sup> - F <sub>c</sub> <sup>2</sup> ) <sup>2</sup>
Data / restraints / parameters	8119 / 371 / 314	8286 / 322 / 237	19087 / 262 / 753
Goodness-of-fit on F <sup>2</sup>	1.015	0.817	1.030
Δ/σmax	0.001	0.001	0.001
Final R indices	5618 data	6004 data	14843 data
[I > 2σ(I)]	R1 = 0.0476, wR2 = 0.0739	R1 = 0.0573, wR2 = 0.1269	R1 = 0.0512, wR2 = 0.1207
R indices [all data]	R1 = 0.0817, wR2 = 0.0867	R1 = 0.0919, wR2 = 0.1553	R1 = 0.0760, wR2 = 0.1396
Largest diff. peak and hole	1.231 and -1.047 eÅ <sup>-3</sup>	2.069 and -1.989 eÅ <sup>-3</sup>	4.756 and -2.752 eÅ <sup>-3</sup>
R.M.S. deviation from mean	0.275 eÅ <sup>-3</sup>	0.455 eÅ <sup>-3</sup>	0.341 eÅ <sup>-3</sup>

<sup>a</sup>  $R = \Sigma ||F_o| - |F_c||/\Sigma|F_o|$ ,  $wR = \{\Sigma[w(|F_o|^2 - |F_c|^2)^2]/\Sigma[w(|F_o|^4)]\}^{1/2}$  and ImEA[SnI<sub>4</sub>],  $w = 1/[\sigma^2(F_o^2) + (0.0167P)^2]$ ; 2-ImEA[SnI<sub>4</sub>],  $w = 1/[\sigma^2(F_o^2) + (0.1000P)^2 + 0.7573P]$ ; HA[SnI<sub>4</sub>],  $w = 1/[\sigma^2(F_o^2) + (0.0588P)^2 + 117.7364P]$  where  $P = (F_o^2 + 2F_c^2)/3$ .

**Table S2.** Crystallographic and structure refinement data for PyrEA[SnI<sub>4</sub>] and 2-PyrEA[SnI<sub>4</sub>].<sup>a</sup>

	Compound	
	PyrEA[SnI <sub>4</sub> ]	2-PyrEA[SnI <sub>4</sub> ]
Empirical formula	C <sub>7</sub> H <sub>12</sub> I <sub>4</sub> N <sub>2</sub> Sn	C <sub>7</sub> H <sub>12</sub> I <sub>4</sub> N <sub>2</sub> Sn
Formula weight	750.48 g mol <sup>-1</sup>	750.48 g mol <sup>-1</sup>
Temperature	100(2) K	100(2) K
Wavelength	0.71073 Å	0.71073 Å
Crystal size	0.020 x 0.100 x 0.120 mm	0.040 x 0.050 x 0.120 mm
Crystal habit	black plate	black needle
Crystal system	orthorhombic	monoclinic
Space group	P b c a	P 1 21/n 1
Unit cell dimensions	a = 17.9119(4) Å α = 90° b = 8.6987(2) Å β = 90° c = 20.3708(5) Å γ = 90°	a = 6.3456(6) Å α = 90° b = 12.4593(11) Å β = 93.2113(19)° c = 19.8832(19) Å γ = 90°
Volume	3173.98(13) Å <sup>3</sup>	1569.5(3) Å <sup>3</sup>
Z	8	4
Density	3.141 g cm <sup>-3</sup>	3.176 g cm <sup>-3</sup>
Absorption coefficient	9.365 mm <sup>-1</sup>	9.470 mm <sup>-1</sup>
F(000)	2640	1320
Theta range for data collection	2.30 to 30.99°	3.27 to 33.77°
Reflections collected	36743	6189
Coverage of independent reflections	100.00 %	99.00 %
Absorption correction	Multi-Scan	Multi-Scan
Max. and min. transmission	0.8350 and 0.3990	0.7030 and 0.3960
Function minimized	Σ w(F <sub>o</sub> <sup>2</sup> - F <sub>c</sub> <sup>2</sup> ) <sup>2</sup>	Σ w(F <sub>o</sub> <sup>2</sup> - F <sub>c</sub> <sup>2</sup> ) <sup>2</sup>
Data / restraints / parameters	5056 / 0 / 128	6189 / 0 / 117
Goodness-of-fit on F <sup>2</sup>	1.053	1.056
Δ/σmax	0.002	0.001
Final R indices	4090 data	4578 data
[I > 2σ(I)]	R1 = 0.0351, wR2 = 0.0755	R1 = 0.0518, wR2 = 0.1183
R indices [all data]	R1 = 0.0484, wR2 = 0.0830	R1 = 0.0799, wR2 = 0.1369
Largest diff. peak and hole	1.977 and -1.094 eÅ <sup>-3</sup>	3.048 and -2.346 eÅ <sup>-3</sup>
R.M.S. deviation from mean	0.205 eÅ <sup>-3</sup>	0.444 eÅ <sup>-3</sup>

<sup>a</sup> R = Σ|F<sub>o</sub>| - |F<sub>c</sub>|/Σ|F<sub>o</sub>|, wR = {Σ[w(|F<sub>o</sub>|<sup>2</sup> - |F<sub>c</sub>|<sup>2</sup>)<sup>2</sup>]/Σ[w(|F<sub>o</sub>|<sup>4</sup>)]}<sup>1/2</sup> and PyrEA[SnI<sub>4</sub>], w = 1/[σ<sup>2</sup>(F<sub>o</sub><sup>2</sup>) + (0.0287P)<sup>2</sup>+16.7852P]; 2-PyrEA[SnI<sub>4</sub>], w = 1/[σ<sup>2</sup>(F<sub>o</sub><sup>2</sup>) + (0.0599P)<sup>2</sup> + 4.7802P]; where P = (F<sub>o</sub><sup>2</sup>+2F<sub>c</sub><sup>2</sup>)/3.

**Table S3.** Crystallographic and structure refinement data for 3-PyrEA[SnI<sub>4</sub>] and 4-PyrEA[SnI<sub>4</sub>].<sup>a</sup>

	Compound	
	3-PyrEA[SnI <sub>4</sub> ]	4-PyrEA[SnI <sub>4</sub> ]
Empirical formula	C <sub>7</sub> H <sub>12</sub> I <sub>4</sub> N <sub>2</sub> Sn	C <sub>7</sub> H <sub>12</sub> I <sub>4</sub> N <sub>2</sub> Sn
Formula weight	750.48 g mol <sup>-1</sup>	750.48 g mol <sup>-1</sup>
Temperature	100(2) K	100(2) K
Wavelength	0.71073 Å	0.71073 Å
Crystal size	0.060 x 0.100 x 0.120 mm	0.020 x 0.060 x 0.200 mm
Crystal habit	black block	black needle
Crystal system	orthorhombic	monoclinic
Space group	P b c a	P 1 21/n 1
Unit cell dimensions	a = 17.5926(4) Å α = 90° b = 8.7826(2) Å β = 90° c = 20.6542(5) Å γ = 90°	a = 6.2823(3) Å α = 90° b = 12.4595(5) Å β = 95.176(2)° c = 20.1704(8) Å γ = 90°
Volume	3191.26(13) Å <sup>3</sup>	1572.39(12) Å <sup>3</sup>
Z	8	4
Density	3.124 g cm <sup>-3</sup>	3.170 g cm <sup>-3</sup>
Absorption coefficient	9.315 mm <sup>-1</sup>	9.452 mm <sup>-1</sup>
F(000)	2640	1320
Theta range for data collection	2.29 to 37.08°	2.60 to 33.74°
Reflections collected	49796	6184
Coverage of independent reflections	99.70 %	99.40 %
Absorption correction	Multi-Scan	Multi-Scan
Max. and min. transmission	0.6050 and 0.4010	0.8330 and 0.2540
Function minimized	Σ w(F <sub>o</sub> <sup>2</sup> - F <sub>c</sub> <sup>2</sup> ) <sup>2</sup>	Σ w(F <sub>o</sub> <sup>2</sup> - F <sub>c</sub> <sup>2</sup> ) <sup>2</sup>
Data / restraints / parameters	8135 / 404 / 197	6184 / 0 / 129
Goodness-of-fit on F <sup>2</sup>	1.042	1.051
Δ/σmax	0.001	0.001
Final R indices	5280 data	4820 data
[I > 2σ(I)]	R1 = 0.0442, wR2 = 0.0901	R1 = 0.0516, wR2 = 0.1159
R indices [all data]	R1 = 0.0806, wR2 = 0.1067	R1 = 0.0780, wR2 = 0.1322
Largest diff. peak and hole	1.898 and -1.645 eÅ <sup>-3</sup>	2.677 and -2.455 eÅ <sup>-3</sup>
R.M.S. deviation from mean	0.233 eÅ <sup>-3</sup>	0.451 eÅ <sup>-3</sup>

<sup>a</sup>  $R = \Sigma \|F_o\| - |F_c\|/\Sigma|F_o\|$ ,  $wR = \{\Sigma[w(|F_o|^2 - |F_c|^2)^2]/\Sigma[w(|F_o|^4)]\}^{1/2}$  and 3-PyrEA[SnI<sub>4</sub>],  $w = 1/[\sigma^2(F_o^2) + (0.0367P)^2 + 5.3113P]$ ; 4-PyrEA[SnI<sub>4</sub>],  $w = 1/[\sigma^2(F_o^2) + (0.0636P)^2]$ ; where  $P = (F_o^2+2F_c^2)/3$

**Table S4.** Metal–halide bond lengths ( $\text{\AA}$ ) in ImEA[SnI<sub>4</sub>]. Red and black colors indicate bonding with terminal and bridging halides, respectively.

Sn1–I2	3.4317(9)	Sn1–I4	3.3388(9)
Sn1–I6	3.1207(9)	Sn1–I6	3.1628(9)
<b>Sn1–I7</b>	<b>2.9607(8)</b>	<b>Sn1–I8</b>	<b>2.9534(9)</b>
Sn2–I3	3.1945(7)	Sn2–I3	3.1945(7)
Sn2–I4	3.1186(6)	Sn2–I4	3.1186(6)
<b>Sn2–I5</b>	<b>3.1272(6)</b>	<b>Sn2–I5</b>	<b>3.1272(6)</b>
<b>Sn3–I1</b>	<b>3.1030(6)</b>	<b>Sn3–I1</b>	<b>3.1030(6)</b>
Sn3–I2	3.1420(6)	Sn3–I2	3.1420(6)
Sn3–I3	3.1939(7)	Sn3–I3	3.1939(7)

**Table S5.** Metal–halide bond lengths ( $\text{\AA}$ ) in 2-ImEA[SnI<sub>4</sub>]. Red and black colors indicate bonding with terminal and bridging halides, respectively.

Sn1–I1	3.1938(19)	Sn1–I1	3.1062(19)
<b>Sn1–I3</b>	<b>2.945(2)</b>	<b>Sn1–I2</b>	<b>2.982(2)</b>
Sn1–I5	3.369(3)	Sn1–I6	3.478(2)
Sn2–I5	3.086(2)	<b>Sn2–I4</b>	<b>3.202(2)</b>
Sn2–I7	3.109(2)	Sn2–I6	3.2149(19)
<b>Sn2–I8</b>	<b>3.079(2)</b>	Sn2–I7	3.240(3)

**Table S6.** Metal–halide bond lengths ( $\text{\AA}$ ) in HA[SnI<sub>4</sub>]. Red and black colors indicate bonding with terminal and bridging halides, respectively.

Sn1–I1	3.2115(14)	Sn1–I2	3.1357(14)
<b>Sn1–I3</b>	<b>2.9816(15)</b>	Sn1–I4	3.0696(17)
Sn1–I7	3.2526(16)	<b>Sn1–I24</b>	<b>3.3597(15)</b>
Sn2–I4	3.1603(16)	Sn2–I5	3.0546(14)
<b>Sn2–I6</b>	<b>3.1620(15)</b>	Sn2–I7	3.0908(15)
Sn2–I9	3.1777(14)	<b>Sn2–I8</b>	<b>3.1513(15)</b>
Sn3–I9	3.1707(14)	<b>Sn3–I10</b>	<b>3.0700(15)</b>
Sn3–I11	3.0875(14)	Sn3–I12	3.1147(16)
<b>Sn3–I23</b>	<b>3.2753(15)</b>	Sn3–I15	3.1936(17)
Sn4–I12	3.2126(16)	<b>Sn4–I13</b>	<b>3.1205(16)</b>

<b>Sn4–I14</b>	<b>3.1753(15)</b>	Sn4–I15	3.0851(16)
Sn4–I1	3.3272(15)	Sn4–I16	2.9984(14)
Sn5–I17	3.0255(17)	Sn5–I20	3.2159(17)
<b>Sn5–I18</b>	<b>2.8990(15)</b>	<b>Sn5–I19</b>	<b>2.9780(15)</b>
Sn5–I16	3.4741(15)	Sn5–I5	3.3743(14)
Sn6–I17	3.2218(17)	Sn6–I2	3.3927(14)
Sn6–I20	2.9971(17)	Sn6–I11	3.2866(15)
<b>Sn6–I21</b>	<b>2.9551(15)</b>	<b>Sn6–I22</b>	<b>3.0219(15)</b>

**Table S7.** Metal–halide bond lengths ( $\text{\AA}$ ) in PyrEA[SnI<sub>4</sub>]. Red and black colors indicate bonding with terminal and bridging halides, respectively.

Sn1–I1	3.1016(5)	Sn1–I1	3.2144(5)
<b>Sn1–I2</b>	<b>2.9558(5)</b>	Sn1–I3	3.0482(5)
Sn1–I3	3.1927(5)	<b>Sn1–I4</b>	<b>3.4835(6)</b>

**Table S8.** Metal–halide bond lengths ( $\text{\AA}$ ) in 2-PyrEA[SnI<sub>4</sub>]. Red and black colors indicate bonding with terminal and bridging halides, respectively.

<b>Sn1–I1</b>	<b>3.2050(10)</b>	Sn1–I2	3.0108(8)
Sn1–I2	3.3181(9)	<b>Sn1–I3</b>	<b>3.0963(10)</b>
Sn1–I4	2.9805(9)	Sn1–I4	3.4092(10)

**Table S9.** Metal–halide bond lengths ( $\text{\AA}$ ) in 3-PyrEA[SnI<sub>4</sub>]. Red and black colors indicate bonding with terminal and bridging halides, respectively.

Sn1–I1	3.0946(4)	Sn1–I1	3.1703(4)
Sn1–I2	3.0888(4)	Sn1–I2	3.1427(4)
<b>Sn1–I3</b>	<b>3.0005(14)</b>	<b>Sn1–I3A</b>	<b>2.942(4)</b>
<b>Sn1–I4</b>	<b>3.3801(6)</b>		

**Table S10.** Metal–halide bond lengths ( $\text{\AA}$ ) in 4-PyrEA[SnI<sub>4</sub>]. Red and black colors indicate bonding with terminal and bridging halides, respectively.

<b>Sn1–I1</b>	<b>3.2489(9)</b>	Sn1–I2	3.2950(9)
<b>Sn1–I3</b>	<b>3.0385(8)</b>	Sn1–I2	3.0368(8)
Sn1–I4	3.2163(8)	Sn1–I4	3.0696(8)

**Table S11.** Metal–halide bond lengths ( $\text{\AA}$ ) in ImEA[PbI<sub>4</sub>]. Red and black colors indicate bonding with terminal and bridging halides, respectively.

Pb1–I1	3.0310(3)	Pb1–I2	3.0268(3)
Pb1–I3	3.1703(3)	Pb1–I3	3.1877(3)
Pb1–I3	3.1877(3)	Pb1–I4	3.3256(3)
Pb2–I4	3.1513(2)	Pb2–I4	3.1513(2)
Pb2–I5	3.1631(3)	Pb2–I5	3.1630(3)
Pb2–I6	3.2329(3)	Pb2–I6	3.2329(2)
Pb3–I6	3.2321(2)	Pb3–I6	3.2321(2)
Pb3–I7	3.1447(3)	Pb3–I7	3.1447(3)
Pb3–I8	3.1864(3)	Pb3–I8	3.1864(3)

**Table S12.** Metal–halide bond lengths ( $\text{\AA}$ ) in 2-ImEA[PbI<sub>4</sub>]. Red and black colors indicate bonding with terminal and bridging halides, respectively.

Pb1–I1	3.1511(16)	Pb1–I1	3.2062(16)
Pb1–I2	3.2533(16)	Pb1–I3	3.1391(16)
Pb1–I3	3.2495(16)	Pb1–I4	3.1258(17)

**Table S13.** Metal–halide bond lengths ( $\text{\AA}$ ) in HA[PbI<sub>4</sub>]. Red and black colors indicate bonding with terminal and bridging halides, respectively.

Pb1–I1	3.2945(3)	Pb1–I2	3.1688(3)
Pb1–I2	3.2573(3)	Pb1–I3	3.1523(3)
Pb1–I3	3.1961(3)	Pb1–I4	3.0532(3)

**Table S14.** Metal–halide bond lengths ( $\text{\AA}$ ) in PyrEA[PbI<sub>4</sub>]. Red and black colors indicate bonding with terminal and bridging halides, respectively.

Pb1–I1	3.2357(5)	Pb1–I2	3.1771(4)
Pb1–I2	3.1658(4)	Pb1–I3	3.1331(5)
Pb1–I4	3.1680(4)	Pb1–I4	3.2238(4)

**Table S15.** Metal–halide bond lengths ( $\text{\AA}$ ) in 2-PyrEA[PbI<sub>4</sub>]. Red and black colors indicate bonding with terminal and bridging halides, respectively.

Pb1–I1	3.1558(4)	Pb1–I2	3.1717(4)
Pb1–I2	3.2045(4)	Pb1–I3	3.1328(4)
Pb1–I3	3.2891(4)	Pb1–I4	3.2223(4)

**Table S16.** Metal–halide bond lengths ( $\text{\AA}$ ) in 3-PyrEA[PbI<sub>4</sub>]. Red and black colors indicate bonding with terminal and bridging halides, respectively.

Pb1–I1	3.1386(14)	Pb1–I2	3.1738(13)
Pb1–I2	3.1777(13)	Pb1–I3	3.2325(14)
Pb1–I4	3.1529(14)	Pb1–I4	3.2075(14)

**Table S17.** Metal–halide bond lengths ( $\text{\AA}$ ) in 4-PyrEA[PbI<sub>4</sub>]. Red and black colors indicate bonding with terminal and bridging halides, respectively.

Pb1–I1	3.1660(19)	Pb1–I1	3.1851(19)
Pb1–I2	3.268(2)	Pb1–I3	3.164(2)
Pb1–I3	3.211(2)	Pb1–I4	3.088(2)

**Table S18.** Metal–halide bond lengths ( $\text{\AA}$ ) in ImEA[PbBr<sub>4</sub>]. Red and black colors indicate bonding with terminal and bridging halides, respectively.

Pb1–Br1	2.9082(4)	Pb1–Br2	2.7735(4)
Pb1–Br3	3.1177(4)	Pb1–Br3	3.2260(4)
Pb1–Br4	3.0242(4)	Pb1–Br4	3.0272(4)

**Table S19.** Metal–halide bond lengths ( $\text{\AA}$ ) in 2-ImEA[PbBr<sub>4</sub>]. Red and black colors indicate bonding with terminal and bridging halides, respectively.

Pb1-Br1	2.9312(14)	Pb1-Br2	2.9446(15)
Pb1-Br2	3.0515(15)	Pb1-Br3	2.8684(17)
Pb1-Br3	3.1748(17)	Pb1-Br4	3.0566(15)

**Table S20.** Metal–halide bond lengths ( $\text{\AA}$ ) in HA[PbBr<sub>4</sub>]. Red and black colors indicate bonding with terminal and bridging halides, respectively.

Pb1–Br2	2.9026(10)	Pb1–Br3	2.9140(10)
Pb1–Br4	2.9371(9)	Pb1–Br1	3.0212(10)
Pb1–Br3	3.0513(10)	Pb1–Br2	3.0917(10)

**Table S21.** Metal–halide bond lengths ( $\text{\AA}$ ) in PyrEA[PbBr<sub>4</sub>]. Red and black colors indicate bonding with terminal and bridging halides, respectively.

Pb1–Br1	2.9294(6)	Pb1–Br1	3.0021(6)
Pb1–Br2	2.8257(7)	Pb1–Br3	2.9973(6)
Pb1–Br3	3.0384(6)	Pb1–Br4	3.2649(8)

**Table S22.** Metal–halide bond lengths ( $\text{\AA}$ ) in 2-PyrEA[PbBr<sub>4</sub>]. Red and black colors indicate bonding with terminal and bridging halides, respectively.

Pb1–Br1	2.9359(14)	Pb1–Br2	2.9344(14)
Pb1–Br2	3.1482(14)	Pb1–Br3	3.0028(13)
Pb1–Br3	3.0160(14)	Pb1–Br4	3.0369(14)

**Table S23.** Metal–halide bond lengths ( $\text{\AA}$ ) in 3-PyrEA[PbBr<sub>4</sub>]. Red and black colors indicate bonding with terminal and bridging halides, respectively.

Pb1–Br1	2.9086(14)	Pb1–Br2	2.9796(11)
Pb1–Br2	2.9934(11)	Pb1–Br3	3.0760(14)
Pb1–Br4	2.9837(12)	Pb1–Br4	2.9872(12)

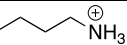
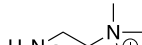
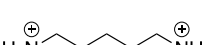
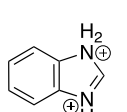
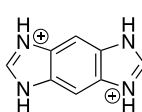
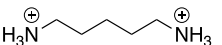
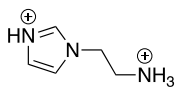
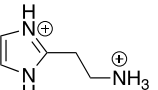
**Table S24.** Metal–halide bond lengths ( $\text{\AA}$ ) in 4-PyrEA[PbBr<sub>4</sub>]. Red and black colors indicate bonding with terminal and bridging halides, respectively.

Pb1–Br1	2.9794(4)	Pb1–Br1	3.0045(4)
Pb1–Br2	3.0723(5)	Pb1–Br3	2.9579(5)
Pb1–Br3	3.0687(5)	Pb1–Br4	2.8841(5)

**Table S25.** List of hybrid 2D perovskites and their respective off-center displacement values.

Compound	Off-center displacement ( $\text{\AA}$ )
2-ImEA[PbBr <sub>4</sub> ]	0.215
2-ImEA[PbI <sub>4</sub> ]	0.153
2-ImEA[SnI <sub>4</sub> ]	0.266 (Sn1) 0.086 (Sn2)
2-PyrEA[PbBr <sub>4</sub> ]	0.087
2-PyrEA[PbI <sub>4</sub> ]	0.105
2-PyrEA[SnI <sub>4</sub> ]	0.196
3-PyrEA[PbBr <sub>4</sub> ]	0.078
3-PyrEA[PbI <sub>4</sub> ]	0.030
3-PyrEA[SnI <sub>4</sub> ]	0.102
4-PyrEA[PbBr <sub>4</sub> ]	0.057
4-PyrEA[PbI <sub>4</sub> ]	0.041
4-PyrEA[SnI <sub>4</sub> ]	0.061
PyrEA[PbBr <sub>4</sub> ]	0.186
PyrEA[PbI <sub>4</sub> ]	0.059
PyrEA[SnI <sub>4</sub> ]	0.189
HA[PbBr <sub>4</sub> ]	0.166
HA[PbI <sub>4</sub> ]	0.159
HA[SnI <sub>4</sub> ]	0.153 (Sn1) 0.066 (Sn2) 0.076 (Sn3) 0.124 (Sn4) 0.310 (Sn5) 0.237 (Sn6)
ImEA[PbBr <sub>4</sub> ]	0.056
ImEA[PbI <sub>4</sub> ]	0.297 (Pb1) 0.000 (Pb2) 0.000 (Pb3) 0.278 (Sn1)
ImEA[SnI <sub>4</sub> ]	0.000 (Sn2) 0.000 (Sn3)

**Table S26.** Intra-octahedral distortion parameters for ImEA[SnI<sub>4</sub>] and 2-ImEA[SnI<sub>4</sub>], plus those of selected previously published (100)- and (110)-oriented Sn-I perovskites.

No.	Organic cation	$\Delta_{oct}$ (x10 <sup>-4</sup> )	$\lambda_{oct}$	$\sigma_{oct}^2$	Reference
1.		0.43	1.0015	4.96	5
2.		0.27	1.0006	2.13	6
3.		2.82	1.0010	2.46	5
4.		1.19	1.0043	14.78	7
5.		0.003	1.0034	12.05	8
6.		21.68	1.0044	7.62	9 <sup>a</sup>
7.		11.41	1.0064	17.88	This work
8.		25.73	1.0096	20.66	This work

<sup>a</sup> “4 × 4” (110)-oriented 2D iodostannate.

Detailed analysis of the X-ray crystal structures of ImEA[SnI<sub>4</sub>] and 2-ImEA[SnI<sub>4</sub>] reveal that their constituent tin-iodide octahedra are significantly more distorted than those in reported (100)- and “4 × 4” (110)-oriented systems. The degree of intra-octahedral distortion can be quantified by comparing the following, previously reported, parameters:<sup>10-13</sup> octahedral elongation ( $\lambda_{oct}$ ), octahedral angle variance ( $\sigma_{oct}^2$ ), and octahedral bond length distortion ( $\Delta_{oct}$ ). The equations for each parameter and an explanation of their meanings can be found above, with larger values corresponding to greater distortion. The greater levels of distortion observed for ImEA[SnI<sub>4</sub>] and 2-ImEA[SnI<sub>4</sub>] are believed to stem from the inherently asymmetric nature of their templating cations, which contain two centres of positive charge (imidazolium core and primary ammonium tail) possessing greatly differing steric profiles. The electrostatic environments around the tin-iodide octahedra are, as a consequence, inherently asymmetric.

**Table S27.** Photovoltaic performance parameters of 10 devices fabricated from 0.50 M solutions (7:3 mixture of DMF and DMSO) of ImEA[SnI<sub>4</sub>].

Samples	$V_{oc}$ (V)	$J_{sc}$ (mA/cm <sup>2</sup> )	$FF$ (%)	$\eta$ (%)
Device 1	0.37	7.34	50.28	1.36
Device 2	0.34	6.91	50.87	1.18
Device 3	0.33	6.85	48.12	1.10
Device 4	0.35	6.15	48.17	1.05
Device 5	0.33	6.56	46.16	0.99
Device 6	0.37	6.48	52.36	1.26
Device 7	0.36	6.20	48.68	1.08
Device 8	0.38	6.35	47.52	1.15
Device 9	0.34	7.45	45.87	1.16
Device 10	0.35	7.25	51.03	1.31

**Table S28.** Photovoltaic performance parameters of 10 devices fabricated from 0.75 M solutions (7:3 mixture of DMF and DMSO) of ImEA[SnI<sub>4</sub>].

Samples	$V_{oc}$ (V)	$J_{sc}$ (mA/cm <sup>2</sup> )	$FF$ (%)	$\eta$ (%)
Device 1	0.45	9.12	55.64	2.26
Device 2	0.42	8.75	57.71	2.12
Device 3	0.41	8.67	60.97	2.19
Device 4	0.40	8.50	56.80	1.92
Device 5	0.42	8.82	55.26	2.03
Device 6	0.40	8.18	53.42	1.74
Device 7	0.44	8.03	50.22	1.77
Device 8	0.41	8.05	56.51	1.85
Device 9	0.39	9.38	54.76	2.01
Device 10	0.44	9.21	54.47	2.19

**Table S29.** Photovoltaic performance parameters of 10 devices fabricated from 1.00 M solutions (7:3 mixture of DMF and DMSO) of ImEA[SnI<sub>4</sub>].

Samples	$V_{oc}$ (V)	$J_{sc}$ (mA/cm <sup>2</sup> )	$FF$ (%)	$\eta$ (%)
Device 1	0.29	6.53	41.51	0.77
Device 2	0.28	6.21	42.09	0.74
Device 3	0.29	5.25	42.87	0.65
Device 4	0.25	6.77	36.78	0.63
Device 5	0.32	6.98	37.13	0.82
Device 6	0.34	7.13	40.55	0.98
Device 7	0.25	6.58	45.03	0.75
Device 8	0.31	7.19	42.79	0.94
Device 9	0.29	5.79	40.22	0.68
Device 10	0.30	6.01	35.63	0.64

## **Discussion on X-ray Photoelectron Spectroscopy results**

As seen in **Figure S18**, Sn exists predominantly in the Sn<sup>II</sup> oxidation state in pristine ImEA[SnI<sub>4</sub>] (with Sn 3d<sub>5/2</sub> and Sn 3d<sub>3/2</sub> peaks at 485.9 eV and 494.3 eV, respectively). The binding energy (BE) of Sn 3d<sub>5/2</sub> electrons in metallic Sn (Sn<sup>0</sup>) is expected to be ~ 485 eV, and > 486 eV in Sn<sup>IV</sup>. The sample was briefly exposed to air during transfer to the UHV system. The absence of surface oxidation suggests that the templating ImEA<sup>2+</sup> organic cations impart some resistance to degradation.

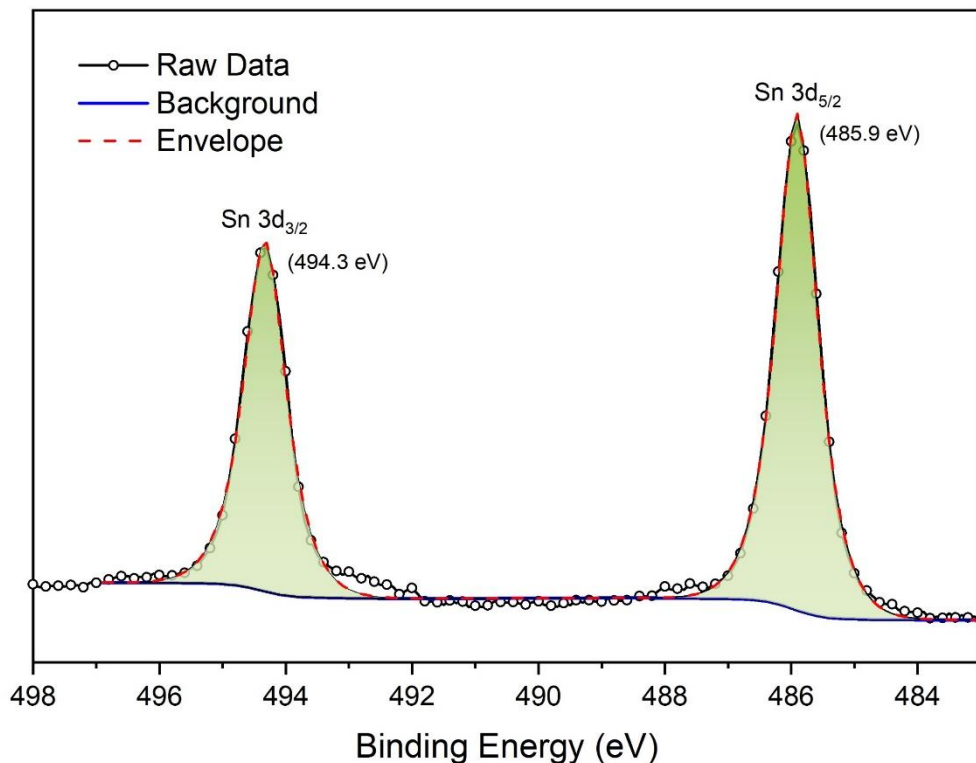


**Figure S18.** Sn 3d core-level XPS spectrum of a pristine thin film of ImEA[SnI<sub>4</sub>] on fluorine-doped tin oxide (FTO) substrate. The sample was prepared in a glovebox, but was briefly exposed to air during transfer into the UHV system of the XPS instrument.

To examine whether the oxidation state of Sn and the perovskite composition varies between the surface and the bulk, the ImEA[SnI<sub>4</sub>] film was subjected to depth profiling by sputtering with Ar gas cluster ions (10 keV Ar<sub>1000</sub><sup>+</sup>), using a raster area of 2 x 2 mm<sup>2</sup>, and an etching time of 30 s for each cycle (n). The evolution of the XPS survey spectra with etching cycle is presented in **Figure S19**. From n = 3 onwards, signals corresponding to the substrate (Sn and O) could be detected but were more pronounced in the last two cycles (n = 4 and 5). The depth profile in the inset of **Figure S19** depicts this most vividly.

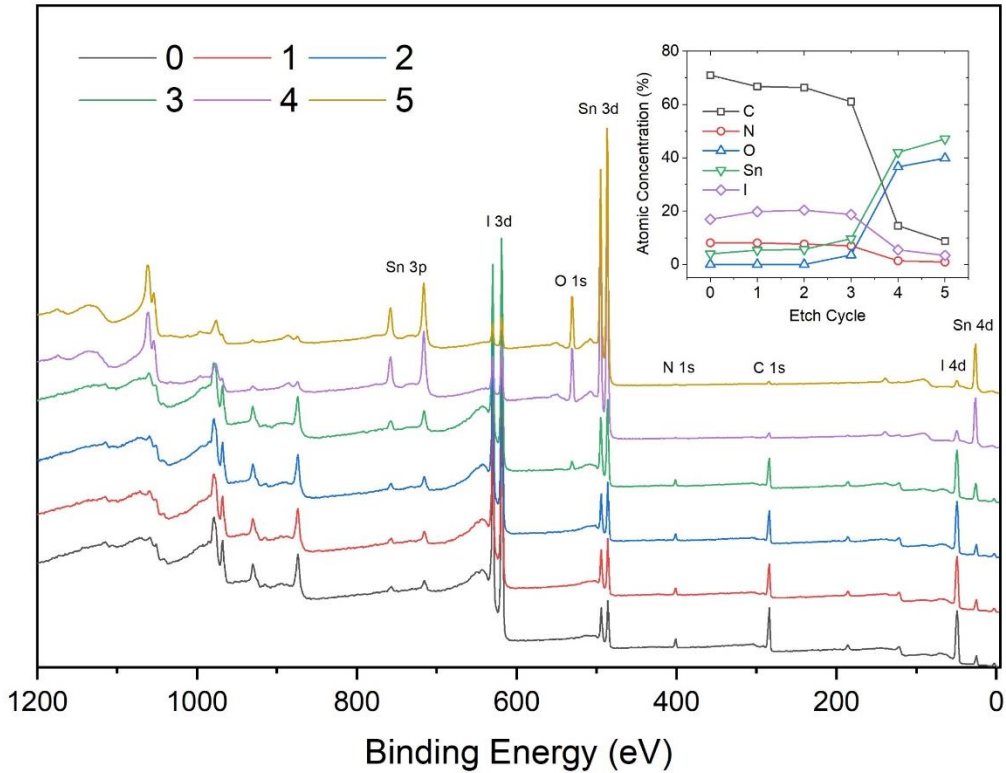


**Figure S19.** XPS survey spectra as a function of etching cycle (“0” corresponds to surface scan, and “n” corresponds to “n<sup>th</sup>” etch cycle). The etching was performed with Ar gas cluster ions (10 keV Ar<sub>1000</sub><sup>+</sup>, etching time of 30s/cycle, over an area of 2 × 2 mm<sup>2</sup>). The inset shows the depth profile of the ImEA[SnI<sub>4</sub>]/FTO sample constructed from the XPS data.

An obvious change in the oxidation state of Sn could be detected in the etch cycle-dependent Sn 3d<sub>5/2</sub> core-level spectra (**Figure S20a**). The spectral features for etch n = 1 and 2 are almost identical to those of the surface scan (n = 0), with Sn<sup>II</sup> as the major component (BE Sn 3d<sub>5/2</sub> ~ 485.9 eV). For n = 3, there is a contribution from both Sn<sup>II</sup> and Sn<sup>IV</sup>, which originate from ImEA[SnI<sub>4</sub>] and FTO, respectively. Spectral deconvolution yields a ratio of Sn<sup>II</sup>: Sn<sup>IV</sup> of 55 %: 45 %. For the last two cycles (n = 4 and 5), only Sn<sup>IV</sup> could be detected. Overall, this data emphasizes the fact that there is no detectable change in the oxidation state of Sn during the brief exposure of the film to air that precedes measurement of the data. Confirmation of the presence of Sn<sup>II</sup> was also obtained by studying the valence band (VB) XPS spectra of the material (**Figure S20b**). For etch cycles n = 0 – 3 the spectral features are very similar to each other, but they are noticeably different to the n = 4 and 5 scans. More specifically, the former (n = 0 – 3) spectra display an additional structure at the lower BE side of the VB (*i.e.*, a prominent structure at 2.6 eV with a shoulder around 1.4 eV), likely due to Sn 5s-derived levels.<sup>14</sup>

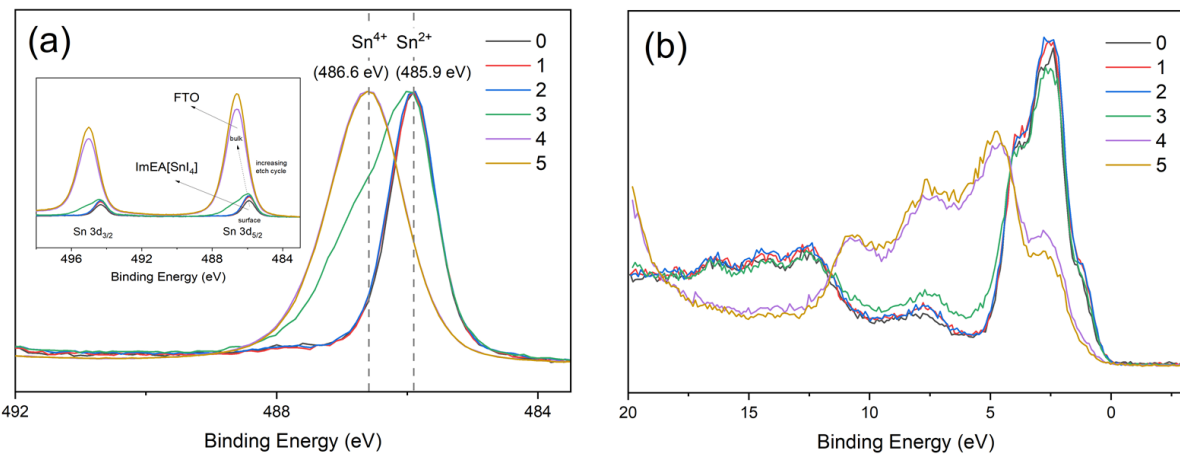


**Figure S20.** a) Normalised Sn 3d<sub>5/2</sub> XPS spectra as a function of etching cycle. The inset shows the complete Sn 3d raw spectra, upon moving from the surface (ImEA[SnI<sub>4</sub>]) to the bulk (FTO). b) XPS valence band spectra as a function of etching cycle.

The XPS calculated elemental composition of thin film ImEA[SnI<sub>4</sub>], as a function of etch cycle, is summarised in **Table S30**. It is likely that the surface scan detects higher levels of carbon due to the presence of “adventitious carbon”, which has a peak that overlaps with that of the sp<sup>3</sup> carbon atoms of the ImEA<sup>2+</sup> moiety. Subsequent etching changes the stoichiometry and leads to a progressive reduction in C, N and I content. This may result from preferential sputtering of the organic groups.<sup>15</sup>

**Table S30.** Composition of 2D tin iodide perovskite ImEA[SnI<sub>4</sub> ], normalised to Sn content. The composition was calculated from high-resolution XPS peak areas of the core-level peaks of the various elements and their relative sensitivity factors (RSFs).

Etch cycle (n)	C	N	Sn	I
0	17.91	2.05	1	4.27
1	12.45	1.51	1	3.70
2	11.75	1.35	1	3.60
3	11.46	1.31	1	3.52

## References

1. Febriansyah, B.; Koh, T. M.; Lekina, Y.; Jamaludin, N. F.; Bruno, A.; Ganguly, R.; Shen, Z. X.; Mhaisalkar, S. G.; England, J. Improved Photovoltaic Efficiency and Amplified Photocurrent Generation in Mesoporous  $n = 1$  Two-Dimensional Lead-Iodide Perovskite Solar Cells. *Chem. Mater.* **2019**, *31*, 890–898.
2. Febriansyah, B.; Lekina, Y.; Ghosh, B.; Harikesh, P. C.; Koh, T. M.; Li, Y.; Shen, Z.; Mathews, N.; England, J. Molecular Engineering of Pure 2D Lead-Iodide Perovskite Solar Absorbers Displaying Reduced Band Gaps and Dielectric Confinement. *ChemSusChem* **2020**, *13*, 2693–2701.
3. Febriansyah, B.; Borzda, T.; Cortecchia, D.; Neutzner, S.; Folpini, G.; Koh, T. M.; Li, Y.; Mathews, N.; Petrozza, A.; England, J. Metal Coordination Sphere Deformation Induced Highly Stokes-Shifted, Ultra Broadband Emission in 2D Hybrid Lead-Bromide Perovskites and Investigation of Its Origin. *Angew. Chem. Int. Ed.* **2020**, *59* (27), 10791–10796.
4. Febriansyah, B.; Giovanni, D.; Ramesh, S.; Koh, T. M.; Li, Y.; Sum, T. C.; Mathews, N.; England, J. Inducing Formation of a Corrugated, White-Light Emitting 2D Lead-Bromide Perovskite *via* Subtle Changes in Templatting Cation. *J. Mater. Chem. C* **2020**, *8* (3), 889–893.
5. Takahashi, Y.; Obara, R.; Nakagawa, K.; Nakano, M.; Tokita, J.; Inabe, T. Tunable Charge Transport in Soluble Organic–Inorganic Hybrid Semiconductors. *Chem. Mater.* **2007**, *19*, 6312–6316.
6. Xu, Z.; Mitzi, D. B.; Medeiros, D. R.  $[(\text{CH}_3)_3\text{NCH}_2\text{CH}_2\text{NH}_3]\text{SnI}_4$ : A Layered Perovskite with Quaternary/Primary Ammonium Dications and Short Interlayer Iodine-Iodine Contacts. *Inorg. Chem.* **2003**, *42*, 1400–1402.
7. Zimmermann, I.; Keene, T. D.; Hauser, J.; Decurtins, S.; Liu, S. X. Crystal Structures of Isotypic Poly[bis-(benz-imid-azolium) [tetra-[ $\mu$ -iodido-stannate(II)]] and poly[bis-(5,6-di-fluoro-benzimidazolium) [tetra-[ $\mu$ -iodido-stannate(II)]]]. *Acta Crystallogr. E* **2014**, *70*, 178–182.
8. Zimmermann, I.; Aghazada, S.; Nazeeruddin, M. K. Lead and HTM Free Stable Two-Dimensional Tin Perovskites with Suitable Band Gap for Solar Cell Applications. *Angew. Chem. Int. Ed.* **2019**, *58*, 1072–1076.
9. Guan, J.; Tang, Z.; Guloy, A. M.  $\alpha$ -[ $\text{NH}_3(\text{CH}_2)_5\text{NH}_3]\text{SnI}_4$ : A New Layered Perovskite Structure. *Chem. Commun.* **1999**, *18*, 1833–1834.

10. Ertl, A.; Hughes, J. M.; Pertlik, F.; Jr., F. F. F.; Wright, S. E.; Brandstatter, F.; Marler, B. Polyhedron Distortions in Tourmaline. *Can. Mineral.*, **2002**, *40*, 153–162.
11. Robinson, K.; Gibbs, G. V.; Ribbe, P. H. Quadratic Elongation: A Quantitative Measure of Distortion in Coordination Polyhedra. *Science* **1971**, *172*, 567–570.
12. Thomas, N. W. Crystal Structure-Physical Property Relationships in Perovskites. *Acta Crystallogr. B* **1989**, *45*, 337–344.
13. Fleet, M. E. Distortion Parameters for Coordination Polyhedra. *Mineral. Mag.* **1976**, *40*, 531–533.
14. Thémlin J.-M.; Chtaïb, M.; Henrard, L.; Lambin, P.; Darville, J.; Gilles, J-M. Characterization of Tin Oxides by X-Ray-Photoemission Spectroscopy. *Phys. Rev. B* **1992**, *46*, 2460–2466.
15. Noël, C.; Pescetelli, S.; Agresti, A.; Franquet, A.; Spampinato, V.; Felten, A.; di Carlo, A.; Houssiau, L.; Busby, Y. Hybrid Perovskites Depth Profiling with Variable-Size Argon Clusters and Monatomic Ions Beams. *Materials* **2019**, *12*, 726.